High-resolution real-time modeling of the marine atmospheric boundary layer in support of the AOSN-II field campaign

James D. Doyle [a,*], Qingfang Jiang [b], Yi Chao [c], John Farrara [c]

[a] Naval Research Laboratory, Marine Meteorology Division, 7 Grace Hopper Avenue, Monterey, CA 93943-5502, USA
[b] UCAR, Monterey, CA, USA
[c] JPL, Caltech, Pasadena, CA, USA

ABSTRACT

The Navy's COAMPS atmospheric model has been used to provide twice-daily, real-time forecasts of 72-h duration in support of the AOSN-II field campaign during August 2003. The model was configured with four grid meshes with a minimum horizontal grid increment of 3 km. A statistical analysis of the model forecasts using available buoy observations demonstrates the skill of the atmospheric model predictions with characteristic wind speed RMS and bias errors of 1–$3\,\mathrm{m\,s^{-1}}$ and less than 0.5–$1.0\,\mathrm{m\,s^{-1}}$, respectively, and temperature RMS errors of 1–$2\,°C$ and biases typically less than $1.0\,°C$. The highest-resolution mesh provides more accurate wind-speed variances during the upwelling periods in the nearshore region, where the wind-speed gradients and diurnal variations are the largest. Persistent and strong low-level winds from a northwesterly direction were associated with a mid-tropospheric trough and jet stream that was substantially stronger than the overall mean monthly conditions. During the relaxation periods, which were relatively infrequent during August 2003, the trough was weaker than the mean conditions with a closed low west of the coast that resulted in southerlies near the coast. During upwelling-favorable conditions, the mean marine inversion was substantially stronger than during the relaxation periods with the surface-stress field exhibiting maxima in the lee of prominent coastal capes and topography, particularly during the periods of strong larger-scale low-level flow. The persistent mean stress pattern that is topographically locked, yields maxima in the stress curl pattern that induce favorable regions of coastal upwelling near and downwind of the coastal promontories and headlands.

Published by Elsevier Ltd.

1. Introduction

Stratified flow within the shallow marine boundary layer along the California coastal mountains often gives rise to a plethora of atmospheric boundary layer phenomena including land/sea breezes (Kindle et al., 2002), low-level jets (Burk and Thompson, 1996), coastal trapped disturbances (e.g., Bond et al., 1996; Thompson et al., 2005), supercritical and transcritical flows (Winant et al., 1988; Rogerson, 1999; Samelson, 1992; Dorman et al., 1999; Tjernström and Grisogono, 2000; Haack et al., 2001), and mesoscale eddies (Bosart, 1983). Some of these disturbances, such as expansion fans, hydraulic jumps, and wakes, may result in sharp gradients in the marine-layer wind speed and wind-stress field thereby creating a complex wind-stress curl pattern that is superimposed on the larger-scale wind-stress curl, which is often favorable for coastal upwelling during the summer periods along the central California coast (Pickett and Paduan, 2003; Chao et al., 2003; Capet et al., 2004). A growing body of literature has documented the skill of high-resolution forecast models in simulating these atmospheric phenomena along coastal regions (e.g., Burk et al., 2000; Kindle et al., 2002; Thompson et al., 2005) and underscored the need for accurate mesoscale atmospheric predictions in order to properly simulate the California coastal ocean circulation (e.g., Marchesiello et al., 2003).

The US West Coast summertime boundary layer has been the subject of numerous studies over the past several decades. The Coastal Ocean Dynamics Experiment (CODE) campaigns (Beardsley et al., 1987; Enriquez and Friehe, 1995) and the Coastal Waves 1996 (Rogers et al., 1998) are examples of such field measurement programs. During the past decade, high-resolution numerical weather prediction models have been applied to explore the complex marine boundary-layer environment along the West Coast (Dorman et al., 1995; Burk and Thompson, 1996; Thompson et al., 1997; Cui et al., 1998). For example, Dorman et al. (2000) documented the mean boundary-layer structure during the summertime along the West Coast, Samelson et al. (2002)

explored the surface-wind conditions near Cape Blanco, OR, during the summer months of 1999, and Koračin et al. (2004) presented complex coastal wind stress and wind-stress curl patterns during summer 1999.

In this study, we present an overview of the atmospheric modeling effort used to provide the high-resolution atmospheric fields in support of a number of ocean modeling studies associated with the Adaptive Ocean Sampling Network II (AOSN-II) field campaign (e.g., Chao et al., 2008; Shulman and Paduan, 2008; Wang et al., 2008; Ramp et al., 2008). This campaign occurred in late summer 2003 in the vicinity of Monterey Bay, California. A unique aspect of this study is the horizontal resolution of the atmospheric model, 3-km, which is significant considering this was performed as part of a real-time effort to support the objectives of AOSN-II. The high-resolution atmospheric forecasts were used to provide the atmospheric forcing for real-time ocean modeling and data assimilation during AOSN-II as described by Chao et al. (2008). The atmospheric forecasts of wind stress and surface fluxes were used by the Innovative Coastal Ocean Observing Network (ICON) model as part of the assimilation system for HF radar-derived currents in the Monterey Bay discussed in Shulman and Paduan (2008). Wang et al. (2008) describes a tidal modeling system in Monterey Bay that made use of COAMPS surface predicted fluxes and stresses. The overview of the AOSN-II program provided by Ramp et al. (2008) describes many of the observational and modeling activities. Also, Ramp et al. (2008) show comparisons of COAMPS high-resolution wind stress and wind-stress curl fields with aircraft derived stresses that attest to the accuracy of the COAMPS near-surface forecasts during AOSN-II.

Our goal of this study is to provide a statistical overview of the atmospheric forecasts performed in support of AOSN-II, and to explore the mean synoptic-scale and mesoscale conditions during the field campaign, particularly contrasting the atmospheric characteristics comprising the upwelling-favorable regime and relaxation periods. The COAMPS modeling system has been applied in real time since summer 2003 over the Central California Coast to provide high-resolution forecasts in support of ocean model activities and maritime interests. It follows that documentation of the model skill will be beneficial for the end users of the real-time system.

A description of the atmospheric model is presented in Section 2. The statistical results are shown in Section 3, followed by mean diagnostic fields in Section 4. The summary and conclusions are presented in Section 5.

2. Atmospheric model description

The atmospheric portion of the Coupled Ocean/Atmosphere Mesoscale Prediction System (COAMPS®) (Hodur, 1997), which is the operational and research mesoscale modeling system of US Navy, was applied in a forecast mode during the AOSN-II field campaign to provide high-resolution winds and surface fluxes for the real-time ocean models. The COAMPS atmospheric model is a finite-difference approximation to the fully compressible, non-hydrostatic equations. Physical parameterizations are used to represent surface fluxes, boundary layer, radiation, and moist processes including microphysical quantities (see Hodur, 1997; Hodur and Doyle, 1998).

The initial fields for the model are created from multivariate optimum interpolation analyses of upper-air sounding, surface, commercial aircraft, and satellite data that are quality controlled and blended with the previous 12-h COAMPS forecast fields. The data assimilation is accomplished through an incremental update procedure that enables mesoscale phenomena to be retained in
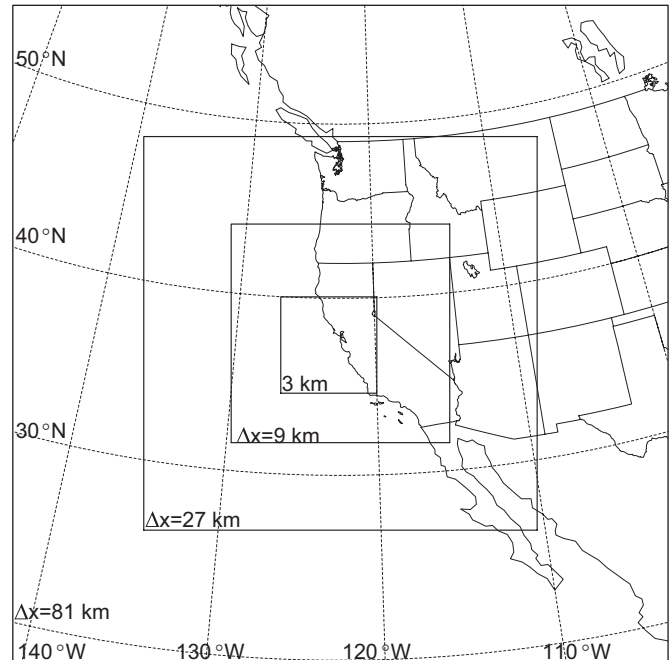

Fig. 1. The domain for the real-time COAMPS forecasts. The horizontal grid increment of the grid meshes are 81-, 27-, 9-, and 3-km resolution.

the analysis increment fields. The lateral boundary conditions for the outermost mesh make use of six-hourly Navy Operational Global Analysis and Prediction System (NOGAPS) forecast fields. The sea-surface temperature analysis is performed directly on the model grid meshes using the NRL Coupled Ocean Data Assimilation System (NCODA), which ingests all available ocean observations in real time, including ship, buoy, and satellite observations.

The domain configuration for these forecasts is shown in Fig. 1 and contains four horizontally nested grid meshes with horizontal grid increments on the computational meshes of 81, 27, 9, and 3 km, respectively. The computational meshes make use of a Lambert conformal projection. The 3-km resolution grid mesh is centered over Central California and the Monterey Bay. The model is configured with 40 vertical levels on a non-uniform vertical grid consisting of an increment of 10 m at the lowest level. The topographic data for the real-data simulations are based on the National Imagery and Mapping Agency (NIMA) 1-km resolution data set that enables the prominent coastal ranges to be well resolved, as shown in Fig. 2 for the 3-km resolution domain. The real-time forecasts were made for a 72-h time period twice daily.

3. Atmospheric model verification

To evaluate the real-time model forecasts from COAMPS, the model results were compared with observations. The most relevant observations for the AOSN-II experiment were the buoys in the vicinity of the Central California Coast. A summary of the model performance relative to the buoy observations at the MBARI moorings 46092 and 46093, commonly referred to as M1 and M2, respectively, and the NOAA buoys at Monterey Bay (46042) and Half Moon Bay (46012) is shown in Fig. 3 (see locations in Fig. 2). The hourly values from 1 to 12 h forecasts were interpolated to the mooring sites for these comparisons.

The buoy time series traces are quite complex with diurnal variations apparent associated with the well-known sea breeze
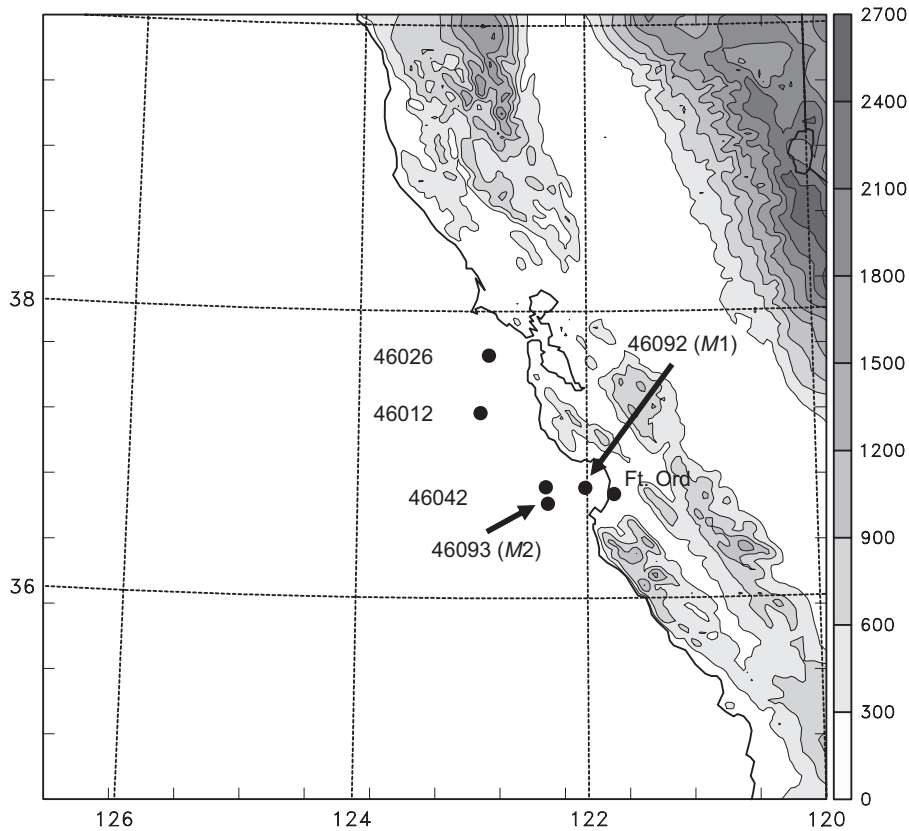
Fig. 2. Terrain (m) for the fourth grid mesh (3-km horizontal resolution) shown at a 300-m interval (gray shading and contours). Buoy and surface station locations of interest are labeled accordingly.

circulation (e.g., Banta et al., 1993; Kindle et al., 2002), as well as modulations on the synoptic time scales. The multi-scale aspects of the Monterey Bay sea breeze has been previously explored by Darby et al. (2002) using atmospheric modeling and lidar observations. They found that the sea-breeze flow was influenced by both the coastal mountain range just east of Monterey Bay and the Sierra Nevada range. The August 2003 AOSN-II field campaign was characterized by rather weak westerly flow during 1–5 August followed by a period of strong northwesterly prevailing winds in the 6–18 August time period. The strong upwelling-favorable wind period was followed by a 4-day period of weaker flow that featured southerly or southwesterly prevailing winds, with stronger winds again at the end of the month. A trend in the temperatures is apparent with the progression of the synoptic-scale systems as well. It is noteworthy that mooring M1 exhibits a greater diurnal cycle associated with the sea/land breeze circulations due to the closer proximity to the shore than M2.

Overall, the model accurately captures the magnitude of the diurnal variations, particularly with respect to the 10-m wind speed. The wind speed trace from 5 to 18 August contains strong low-level winds with diurnal signatures of the multi-scale sea breeze apparent. The wind-speed perturbations associated with the sea-breeze circulation reach as much as $10 \, \mathrm{m \, s^{-1}}$. The model occasionally appears to over-predict the wind speed minima that are a signature of the sea/land breeze diurnal cycle, such as during the 12–14 August time period at 46092 and 46093. It is interesting to note that the diurnal wind-speed cycle is much stronger at 46092 and 46093 than the NOAA buoys 46042 and 46012. One would expect the diurnal signature to be strong at 46092, since it is the closest observation to the shore. Although buoys 46042 and 46093 are quite close in proximity, occasionally some significant differences between the two occur in the diurnal cycle behavior,

such as exhibited by the winds during the 17–18 August time period. The model appears to contain 1–3 °C temperature errors from 14 to 18 August, particularly for the 46092 mooring, which is coincident with the passage of a synoptic-scale trough and near the time when the flow changed from upwelling favorable to a relaxation state. It should be noted that there are periods of time when the COAMPS analysis contains a positive sea-surface temperature bias error that contributes to some of the bias in the near surface air temperature. As an example, the sea surface temperature time series for August for the 46093 mooring (M2) as well as the COAMPS 3-km analyses, shown in Fig. 4, indicates a positive bias of 1–1.5 °C for several extended periods of time. Some of the bias may be a result of cloud issues that prevent the use of satellite observations in the COAMPS sea-surface temperature analysis.

The statistical performance of the model with regard to bias and root-mean-square error for moorings 46093, 46092, 46012, 46026 (San Francisco site), and 46042 is summarized in Tables 1–5, respectively. The model forecasts for the 3- and 9-km resolution grid meshes have been stratified into 12 hourly forecast periods for the 72-h forecasts, which were performed twice daily during the field campaign. There are a number of interesting trends in these statistics. The temperature and wind speed RMS errors generally increase with forecast lead time for all buoys, which is what one would expect from a forecast error growth perspective. However, it is surprising that this error growth is rather small. The temperature RMS errors are consistently less than 1.5 °C with the exception of 46092, which is the nearest to shore and exhibits slightly larger RMS errors of 1.5–2.0 °C. The temperature bias is generally less than 1.0 °C, with most of the statistics showing a negative or warm bias in the 2-m temperatures.
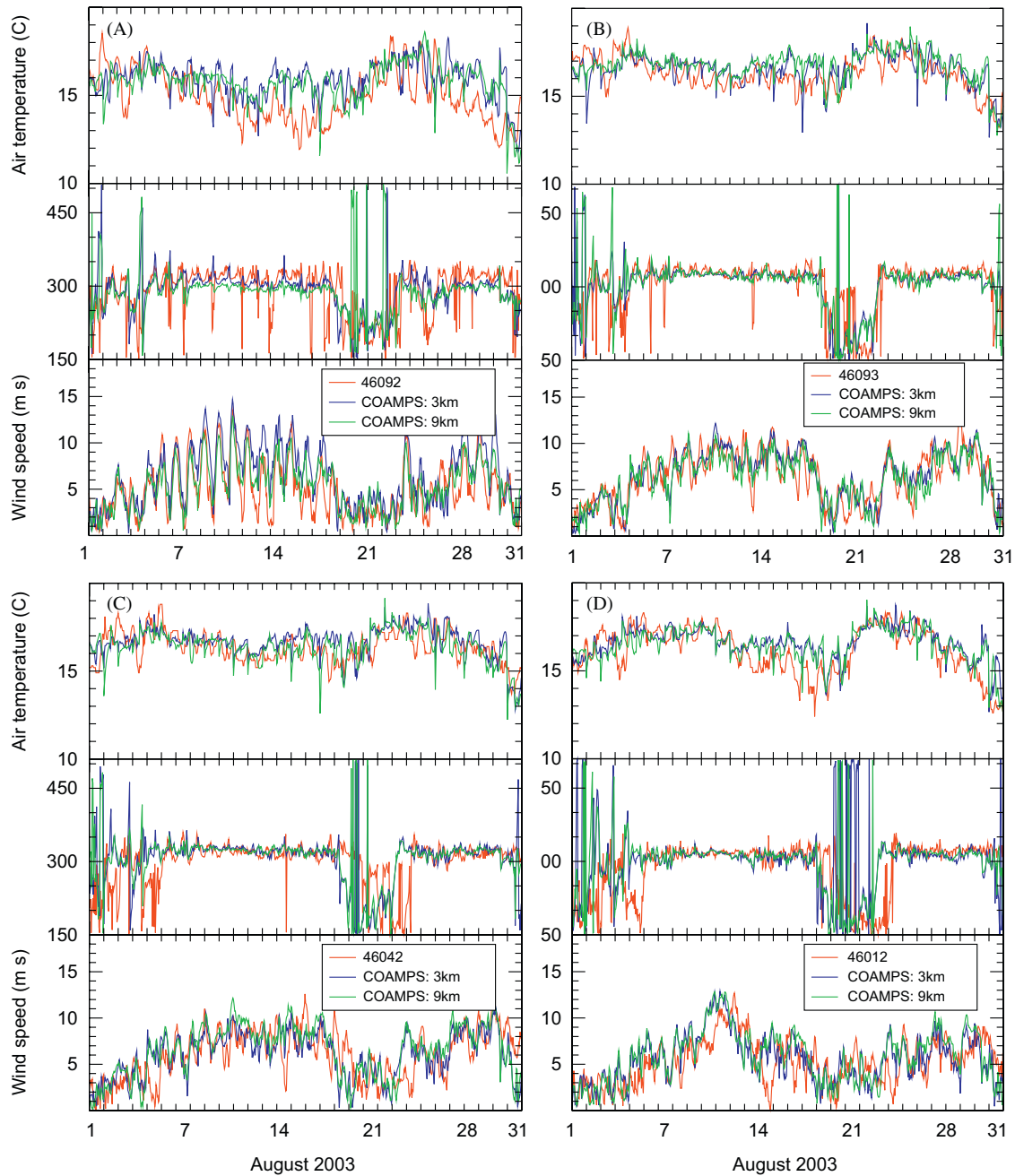
Fig. 3. Time series of the air temperature (°C) (top panel), wind direction (°) (middle panel), and wind speed (m s^{-1}) (bottom panel) for the buoy observations (red), COAMPS 3 km mesh (blue) and COAMPS 9-km mesh (green) (1–12 h forecasts) for August 2003. The buoys shown are: (A) 46092 (MBARI mooring site 1, M1), (B) 46093 (MBARI mooring site 2, M2), (C) 46042 (Monterey Bay), and (D) 46012 (Half Moon Bay). The locations are shown in Fig. 2.

The 10-m wind speed RMS error also exhibits an increase with forecast time similar to the temperature statistics. However, once again the error growth is small relative to RMS wind-speed errors aloft and overall the RMS error is generally less than 2.5–3.0 m s^{-1}. Interestingly, the wind-direction RMS errors appear to be nearly independent of forecast lead time. The wind-speed bias is less than 0.5 m s^{-1} at 46093 and 46042 and slightly larger at the other sites with no obvious systematic trend. The wind-direction bias is typically less than 10°.

The statistics shown in Tables 1–6 summarize the performance for both the 3- and 9-km resolution grid meshes. Statistically, the performance of the 3- and 9-km meshes is nearly identical. Verification and evaluation of high-resolution model forecasts is certainly a major challenge and the subject of an active

community of research (e.g., Baldwin et al., 2002; Nachamkin et al., 2005). Special mesoscale verification procedures (e.g., Nachamkin, 2004) are likely needed to systematically distinguish the subtle but significant forecast skill differences between the 3- and 9-km meshes. Nachamkin et al. (2007) examined atmospheric forecasts from meshes with 1- and 27-km horizontal grid increments. Although the forecasts from the 1-km mesh exhibited more detail than those on the 27-km grid, the RMS and bias verification statistics were quite similar. However, statistics derived from dispersion forecasts showed that the 1-km atmospheric forcing produced more accurate trajectories than the 27-km output when compared to the dosage measurements. It follows that although the 3- and 9-km mesh statistics are similar based on the sparsely spaced buoy network, one cannot conclude
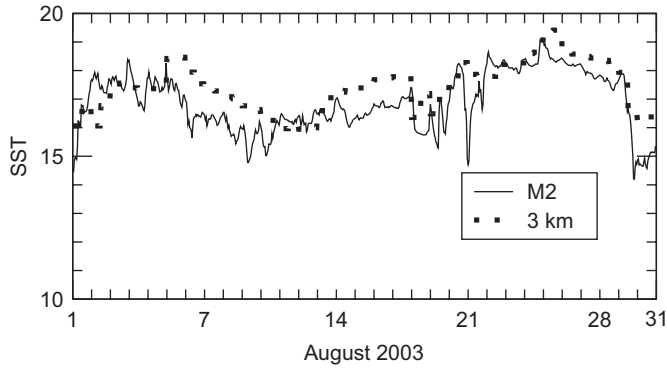
Fig. 4. Time series of the sea-surface temperature (°C) for the 46093 (MBARI mooring site 2, M2) observations (solid) and the COAMPS 3 km mesh (dots) for August 2003. The sea-surface temperatures are analyzed in COAMPS every 12 h and held constant during the twice-daily forecasts.

Table 1
Verification statistics comparing the 3- and 9-km resolution COAMPS meshes with the 46093 mooring

Forecast period (h)	BIAS			RMS		
	Direction (°)	Speed (m s⁻¹)	Temp (°C)	Direction (°)	Speed (m s⁻¹)	Temp (°C)
46093 3 km						
1–12	−3.1	0.1	−0.5	40	1.8	0.9
13–24	−0.5	0.3	−0.6	41	1.9	1.0
25–36	−2.5	0.3	−0.5	41	1.9	1.0
37–48	−5.0	0.5	−0.4	43	2.1	1.1
49–60	−4.4	0.4	−0.5	41	2.1	1.2
61–72	−5.2	0.4	−0.5	40	2.1	1.3
46093 9 km						
1–12	−2.6	−0.2	−0.2	39	1.7	0.8
13–24	−1.8	0.0	−0.4	39	1.8	0.9
25–36	−3.3	0.1	−0.4	43	1.9	0.9
37–48	−10.0	0.1	−0.4	45	2.0	1.0
49–60	−5.8	0.0	−0.4	45	2.1	1.1
61–72	−3.5	0.1	−0.4	37	2.1	1.2

The bias statistics are computed based on the difference between the buoy and model (buoy-model).

Table 2
As in Table 1 except for the 46092 mooring

Forecast period (h)	BIAS			RMS		
	Direction (°)	Speed (m s⁻¹)	Temp (°C)	Direction (°)	Speed (m s⁻¹)	Temp (°C)
46092 3 km						
1–12	−3.2	−1.5	−0.9	47	2.6	1.6
13–24	−3.6	−1.3	−1.0	48	2.7	1.6
25–36	−3.2	−1.2	−1.0	46	2.7	1.6
37–48	−3.9	−1.1	−1.0	46	2.6	1.7
49–60	−2.5	−1.0	−1.0	47	2.5	1.8
61–72	−5.5	−0.9	−1.0	48	2.5	1.8
46092 9 km						
1–12	0.1	−0.4	−0.8	46	1.8	1.6
13–24	0.5	−0.1	−0.9	43	1.8	1.7
25–36	9.0	0.0	−1.0	44	2.0	1.7
37–48	−1.7	0.1	−1.0	46	1.9	1.7
49–60	1.3	0.1	−1.0	46	1.9	1.8
61–72	0.7	0.0	−1.0	46	2.0	1.9

Table 3
As in Table 1 except for the 46012 mooring

Forecast period (h)	BIAS			RMS		
	Direction (°)	Speed (m s⁻¹)	Temp (°C)	Direction (°)	Speed (m s⁻¹)	Temp (°C)
46012 3 km						
1–12	−15.0	−0.3	−0.5	45	1.7	1.3
13–24	−15.0	−0.2	−0.5	47	1.7	1.3
25–36	−17.0	−0.2	−0.5	45	1.8	1.4
37–48	−18.0	−0.2	−0.3	46	1.9	1.6
49–60	−16.0	−0.3	−0.4	45	2.1	1.6
61–72	−18.0	−0.4	−0.4	43	2.4	1.7
46012 9 km						
1–12	−8.7	−0.6	−0.4	38	1.9	1.2
13–24	−16.0	−0.5	−0.5	45	1.8	1.3
25–36	−18.0	−0.5	−0.4	44	2.1	1.4
37–48	−17.0	−0.5	−0.3	44	2.1	1.6
49–60	−20.0	−0.6	−0.3	46	2.4	1.7
61–72	−22.0	−0.7	−0.3	47	2.6	1.8

Table 4
As in Table 1 except for the 46026 mooring

Forecast period (h)	BIAS			RMS		
	Direction (°)	Speed (m s⁻¹)	Temp (°C)	Direction (°)	Speed (m s⁻¹)	Temp (°C)
46026 3 km						
1–12	−6.3	−1.3	−0.8	39	2.4	1.4
13–24	−5.6	−1.2	−0.8	41	2.5	1.4
25–36	−5.6	−0.9	−0.7	42	2.5	1.5
37–48	−9.9	−0.8	−0.6	43	2.5	1.6
49–60	−11.0	0.9	−0.7	45	2.6	1.7
61–72	−5.8	−1.2	−0.6	46	2.8	1.8
46026 9 km						
1–12	−4.8	−1.8	−0.4	41	2.9	1.3
13–24	−1.5	−1.6	−0.4	40	2.8	1.3
25–36	−4.7	−1.3	−0.4	42	2.8	1.4
37–48	−8.0	−1.2	−0.4	44	2.7	1.6
49–60	−5.2	−1.2	−0.4	43	2.8	1.8
61–72	−3.2	−1.5	−0.4	43	3.0	1.9

Table 5
As in Table 1 except for the 46042 mooring

| Forecast period (h)	BIAS			RMS		
	Direction (°)	Speed (m s⁻¹)	Temp (°C)	Direction (°)	Speed (m s⁻¹)	Temp (°C)
46042 3 km						
1–12	−6.9	0.0	−0.3	40	1.7	1.0
13–24	−5.6	0.2	−0.5	44	1.8	0.9
25–36	−8.6	0.3	−0.4	39	1.8	1.0
37–48	−14.0	0.4	−0.3	41	1.9	1.1
49–60	−11.0	0.3	−0.4	40	2.0	1.2
61–72	−12.0	0.3	−0.4	38	2.0	1.2
46042 9 km						
1–12	−7.8	−0.4	−0.1	40	1.8	0.9
13–24	−7.1	−0.2	−0.2	39	1.7	0.9
25–36	−9.1	−0.1	−0.2	39	1.8	0.9
37–48	−15.0	−0.1	−0.2	40	1.9	1.0
49–60	−11.0	−0.1	−0.2	41	2.0	1.1
61–72	−7.9	−0.1	−0.2	36	2.1	1.2

Table 6
Averaged verification statistics comparing the 3- and 9-km resolution COAMPS meshes with the 46092, 46093, 46042, 46012, 46026 moorings

Forecast period (h)	BIAS			RMS		
	Direction (°)	Speed (m s^{-1})	Temp (°C)	Direction (°)	Speed (m s^{-1})	Temp (°C)
3 km						
1–12	−5.8	−0.5	−0.5	35.5	1.7	1.0
13–24	−5.1	−0.4	−0.6	37.0	1.8	1.1
25–36	−6.2	−0.3	−0.5	35.7	1.8	1.1
37–48	−8.4	−0.2	−0.5	36.5	1.8	1.2
49–60	−7.4	−0.2	−0.5	36.3	1.9	1.3
61–72	−7.8	−0.3	−0.5	35.8	2.0	1.3
Total	−8.1	−0.4	−0.6	43.4	2.2	−0.6
9 km						
1–12	−4.0	−0.6	−0.3	34.1	1.7	1.0
13–24	−3.3	−0.4	−0.4	34.4	1.7	1.0
25–36	−4.4	−0.3	−0.4	35.4	1.8	1.1
37–48	−8.7	−0.3	−0.4	36.7	1.8	1.2
49–60	−6.9	−0.3	−0.4	36.8	1.9	1.3
61–72	−6.0	−0.4	−0.4	34.8	2.0	1.3
Total	−6.6	−0.4	−0.5	42.4	2.1	−0.5

that the forecasts are of equal skill, particularly when used to force other models such as ocean circulation or dispersion. The ocean modeling community appears to have anecdotal evidence that the high-resolution meshes, such as the 3-km resolution grid, are more skillful and able to more realistically represent the alongshore wind stress (Capet et al., 2004) and wind-stress curl (Kindle et al., 2002; Pickett and Paduan, 2003). Accurate atmospheric forcing is critical for the skillful ocean predictions during AOSN-II (e.g., Haley et al., 2008). Although the statistics are rather neutral with respect to resolution, the typical differences as a function of model resolution are highlighted in Fig. 5, which is a 48-h forecast of 10-m wind speed and vectors valid at 00 UTC 5 September 2003. The coastal jet structures present along the prominent coastal capes are better resolved in the high-resolution 3-km mesh than the 9- or 27-km grids. Additionally, the wind-speed gradient across the shore is better defined in the high-resolution meshes. The 27-km mesh fails to capture much of the wind flow structure along the coast. Thus, although the statistics including the mean skill scores (e.g. Table 6) indicate similarities between the 3- and 9-km meshes, numerous individual forecasts indicate that much more realistic structure in the low-level wind and temperature fields is apparent in the highest-resolution mesh. We also note that the buoy network in the Monterey Bay is limited; moorings 46092 and 46093 may not be optimally located to clearly differentiate the advantages of high horizontal resolution for time scales greater than the diurnal cycle. The two buoys are really insufficient to resolve the fine-scale structures present in the 3-km winds. For example, the winds in the 3-km mesh are stronger immediately along the Santa Cruz headlands coast, in contrast to the 27- and 9-km meshes, which have more of a gradual gradient between the coast and the higher wind speeds offshore. These nearshore gradients in stress and wind speed can be important for ocean models.

The forecast wind-speed variance interpolated to the M1 buoy site is significantly larger for the 3-km mesh than the 9-km, 10.6 m^2 s^{-2} versus 6.0 m^2 s^{-2} during the upwelling periods. The observed wind-speed variance at M1 during the upwelling periods is 9.4 m^2 s^{-2}. Farther offshore, the variances for the 3- and 9-km meshes at M2 are statistically similar and smaller in magnitude, 5.1 and 5.8 m^2 s^{-2}, respectively; both of which
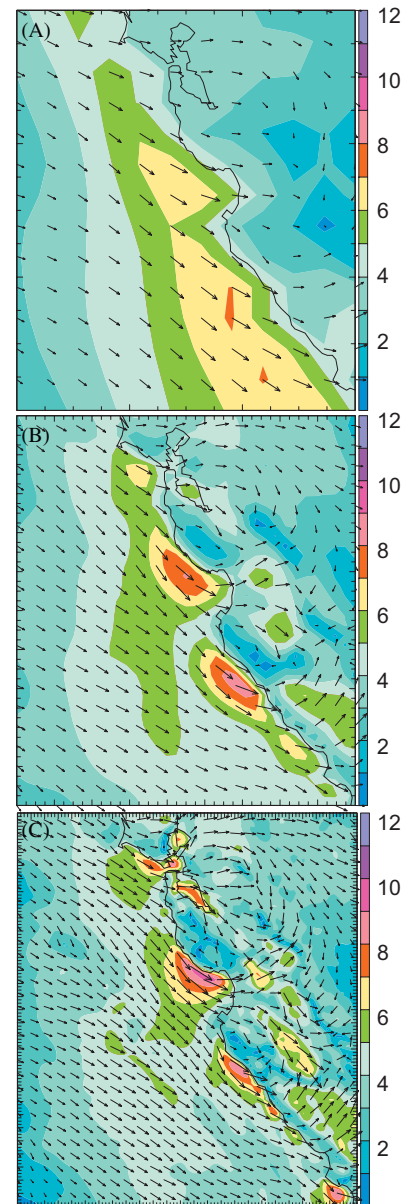
Fig. 5. The 10-m wind speed (interval 1 m s^{-1}) and vectors valid at 00Z 5 September 2003 (48 h forecast) from the (A) 27-km, (B) 9-km and (C) 3-km grid meshes.

compare well with the M2 wind-speed variance of 6.2 m^2 s^{-2}. Thus, the high-resolution mesh does provide more accurate wind-speed variance information during the upwelling periods in the nearshore region, where the wind-speed gradients and diurnal variations are the largest.

It is noteworthy that Shulman et al. (2007) investigated the upwelling and relaxation events during AOSNI, which took place in August and September of 2000, using the Navy Coastal Ocean Model (NCOM) forced by the COAMPS forecast fields. They found the COAMPS short-wave radiation to be overestimated by approximately 40% through analysis of the Photosynthetically Available Radiation (PAR) measurements at the MBARI moorings 46092 and 46093. This is likely an indication that COAMPS did not produce sufficient low-level clouds during this time period. We also made similar comparisons and noted that COAMPS appears to overestimate the shortwave radiation during some periods particularly late in the month due to an underestimate of
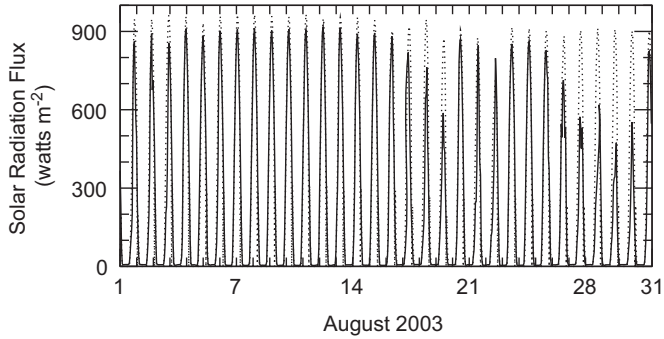
Fig. 6. Time series of shortwave radiation observations (W m^{-2}) from the Fort Ord surface observations and the 1–12 h forecasts from the COAMPS 3 km mesh (dots) for August 2003.

low-level clouds. For example, a time series of shortwave radiation observations, shown in Fig. 6, indicates marked over-prediction of the shortwave radiation at the Fort Ord NPS observation site during several periods of stratus clouds, particularly in the 18–20 and 27–30 August time periods. Any bias in the simulated low-level clouds undoubtedly will have an impact of the net long wave radiation as well. The underprediction of low-level clouds is also consistent with the low-level warm bias apparent in the mean temperature statistics (e.g., Table 6).

4. Mean atmospheric forecast diagnostics

Given the general skill of our model, it is appropriate to perform additional diagnosis using the model data to gain a better understanding of the upwelling and relaxation signatures that are prominent in the time series shown in Fig. 3. Mean quantities of near-surface model fields are available at a 1-h interval, and the standard model fields on the terrain following surfaces are available every 3 h. The averages have been computed for various fields for the entire month of August 2003. Also, averages have been stratified for the upwelling-favorable and relaxation periods. We distinguish upwelling and relaxation periods using the 46092 mooring. The upwelling periods are designated as when the daily mean of the northerly wind component (positive defined as a flow from the north to south) was equal to or exceeded 5 m s^{-1} at the 46092 mooring, and the relaxation periods when the daily mean was less than 5 m s^{-1}. This yields a total of 23 upwelling days and 8 relaxation days. The relaxation regime periods are 1–5 August and 20–22 August. Examination of the 46092 low-pass filtered time series of the winds (see Fig. 2 in Ramp et al., 2008) indicates that the strong winds arriving from a northwesterly direction dominated the upwelling period and provides qualitative justification for the upwelling and relaxation definition.

In order to better understand the mean synoptic-scale conditions during the AOSN-II field campaign, the 500-hPa winds and geopotential height were averaged for the 27-km resolution grid mesh (second mesh) and is shown in Fig. 7. The mean conditions during August 2003 (Fig. 7A) were characterized by a large-scale trough positioned to the west of the California coastline and a broad region of southwesterly flow. These conditions are typical for the summertime conditions for the US West Coast as indicated by the mean geopotential height derived from the NCEP/NCAR reanalysis using a horizontal resolution of 2.5° (Kalnay et al., 1996). A large-scale trough was centered near 130°W with a ridge axis near 105°W during August 2003 (Fig. 8A). The position of the trough and ridge axis is similar to the 20 yr climatological August conditions (Fig. 8B), although the trough
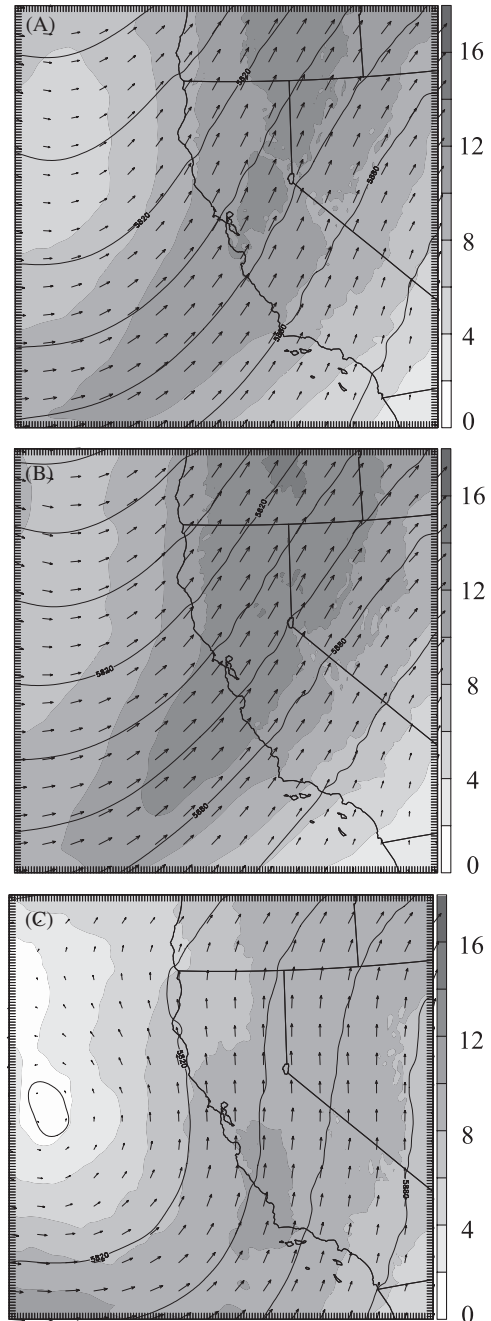
Fig. 7. The 500-hPa geopotential height (interval every 20 m) and wind speed (gray shading interval 2 m s^{-1}) for the (A) August 2003, (B) upwelling-favorable, and (C) relaxation dominated time periods for the second grid mesh (27-km resolution).

was significantly deeper than the climate mean, leading to stronger low-level pressure gradients and a more vigorous near-surface northwesterly flow.

The synoptic-scale conditions for the upwelling-favorable regime, shown in Fig. 7B, indicate that the synoptic-scale trough and jet stream were considerably stronger during the strong onshore wind periods. The stronger mid-tropospheric trough is consistent with a strong low-level pressure gradient that drives the persistent northwesterly flow along the Central California coast. In contrast, during the relaxation periods, the mean 500-hPa heights and winds indicate a weakening of the synoptic-scale trough and more of a southerly flow in the middle

(A)

(B)
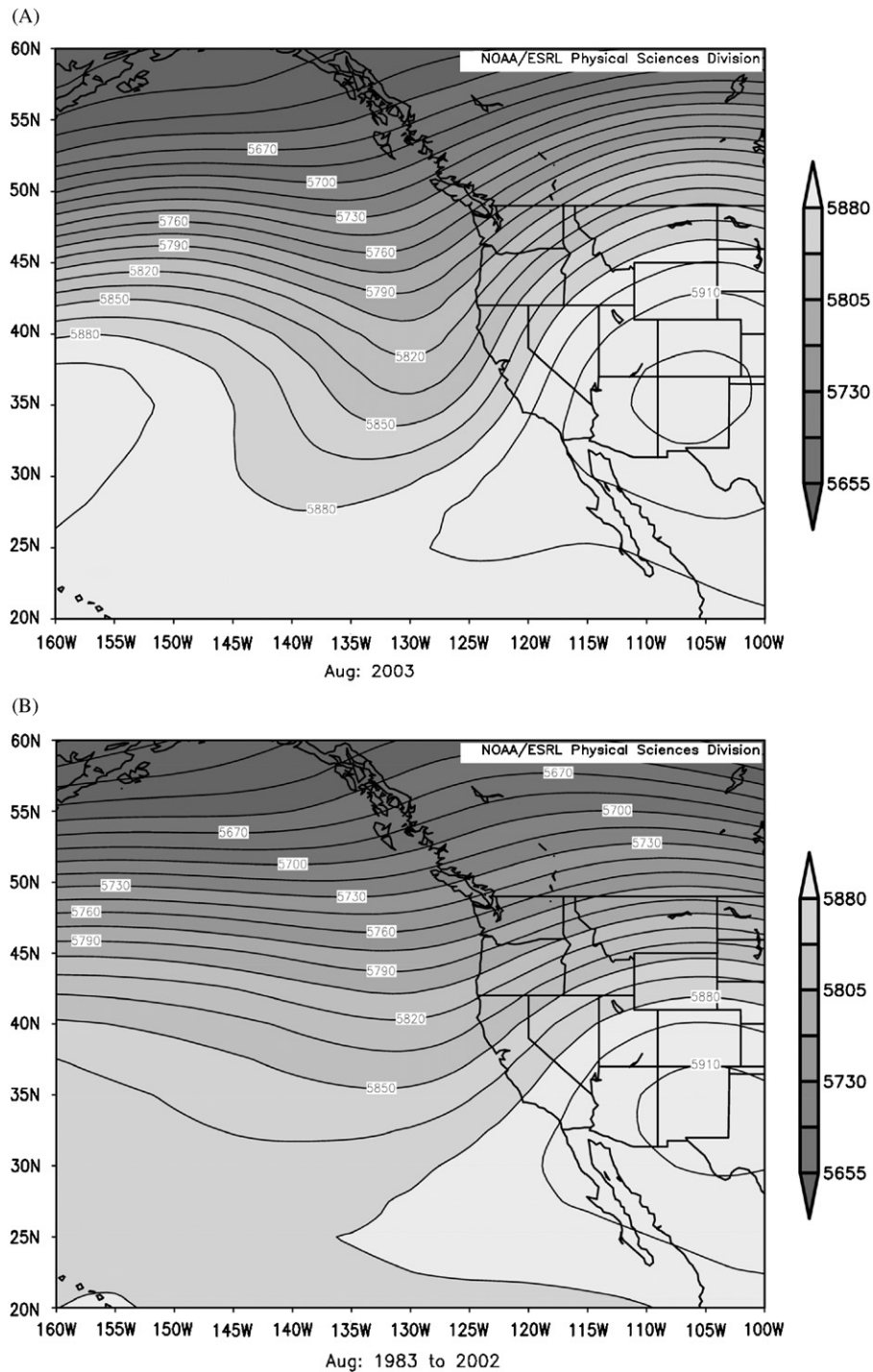
Fig. 8. The 500-hPa geopotential height mean (interval every 15 m) for the (A) August 2003, and (B) August 1983–2002 time periods using the NCEP/NCAR reanalysis (derived from the NOAA/ESRL Physical Sciences Division analysis software).

troposphere (Fig. 7C). The general weakness in the middle-level geopotential height gradient is consistent with weaker pressure gradients near the surface and weaker wind conditions.

The mean 10-m wind speed and wind vectors are shown in Fig. 9 for the August time period based on the 3-km COAMPS winds. The mean conditions for the entire month (Fig. 9A) show northwesterly flow along the coast of 5–10 m s^{-1}. The upwelling-favorable mean wind speed is strong (Fig. 9B), as one would expect, with local enhancements downwind of local promontories such as south of Point Sur and Santa Cruz. These features are
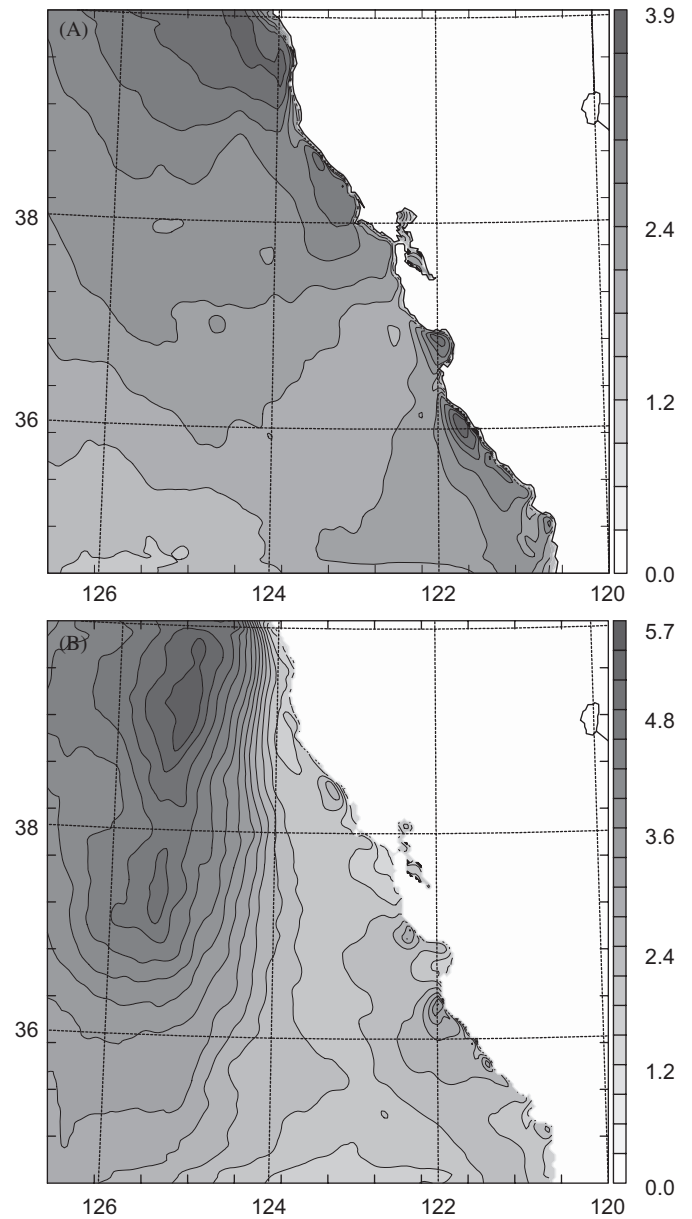
consistent with hydraulically forced accelerations associated with adjustments to the flow around the complex coastline, as discussed in the literature (e.g., Rogerson, 1999; Haack et al., 2001; Dorman et al., 2000). During the relaxation periods, the low-level flow is substantially weaker and is characterized by very weak gradients in the wind speed (Fig. 9C). Some enhancement of the low-level wind speed is still apparent along some coastal locations and within the Monterey Bay. The standard deviations of the mean wind speed for the upwelling and relaxation regimes are shown in Fig. 10. The standard deviation for the upwelling
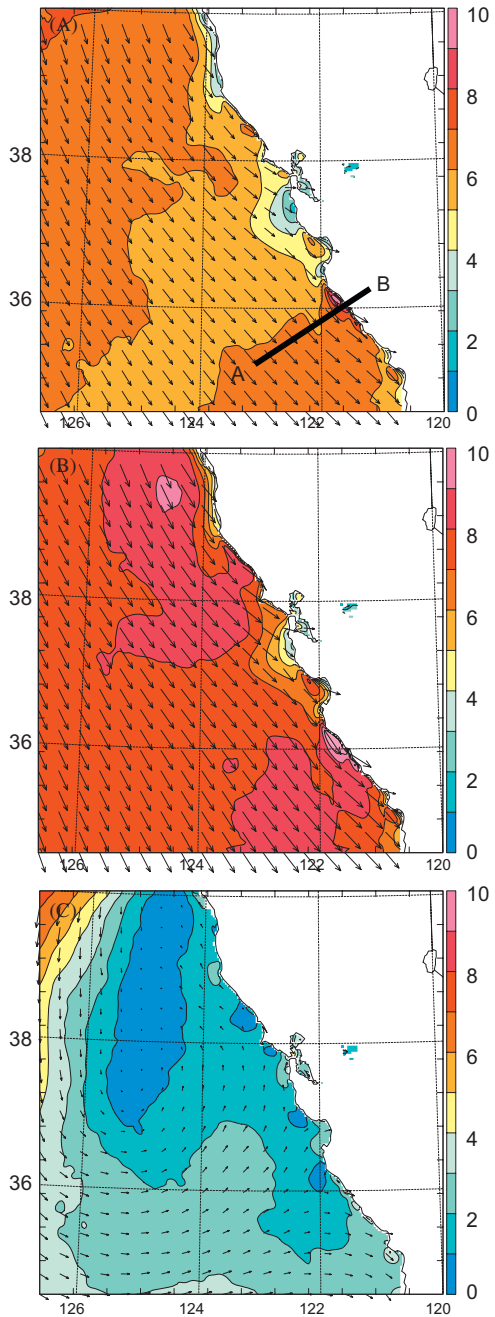
Fig. 9. The 10-m wind speed (every 1 m s^{-1}) and wind vectors for the (A) August 2003, (B) upwelling-favorable, and (C) relaxation dominated time periods for the fourth grid mesh (3-km resolution).


Fig. 10. Standard deviation of the wind speed (m s^{-1}) for the (A) upwelling and (B) relaxation regime time periods. The contour and gray shading interval is 0.3 m s^{-1}.

regime (Fig. 10A) indicates variance maxima near the coastal wind-speed jets along the Big Sur coast, within the Monterey Bay, and offshore and downwind of the Pt. Arena headlands. The maxima in the standard deviation correspond to spatial variations in the location of the wind-speed gradients, particularly in Monterey Bay, as well as variations in the maxima corresponding to the coastal jets, such as downwind of Pt. Sur. Some of the coastal jet features are more or less forced by the coastal terrain and therefore do not vary much spatially. In contrast, the wind-speed standard deviation for the relaxation regime (Fig. 10B) contains fewer gradients along the coast with the exception of near Pt. Sur and the Santa Cruz headlands, possibly

associated with occasional southerly flow events that interact with the coastal promontories. A large variance maximum is located offshore and is associated with the mean trough position and synoptic-scale induced variability in the low-level winds.

Vertical cross sections of the mean potential temperature and coast parallel wind speed, constructed along the A–B plane (see Fig. 9A), are shown in Fig. 11. A well-defined marine inversion layer is apparent in the mean field for the entire month of August (Fig. 11A), with a more shallow inversion positioned immediately along the coast, typical of the California summertime boundary layer structure (e.g., Rogers et al., 1998; Dorman et al., 2000). In the upwelling-favorable regime (Fig. 11B), the marine boundary-layer inversion is substantially stronger than the overall background conditions, with a considerably stronger along coast wind component. The relaxation period conditions (Fig. 11C) feature a
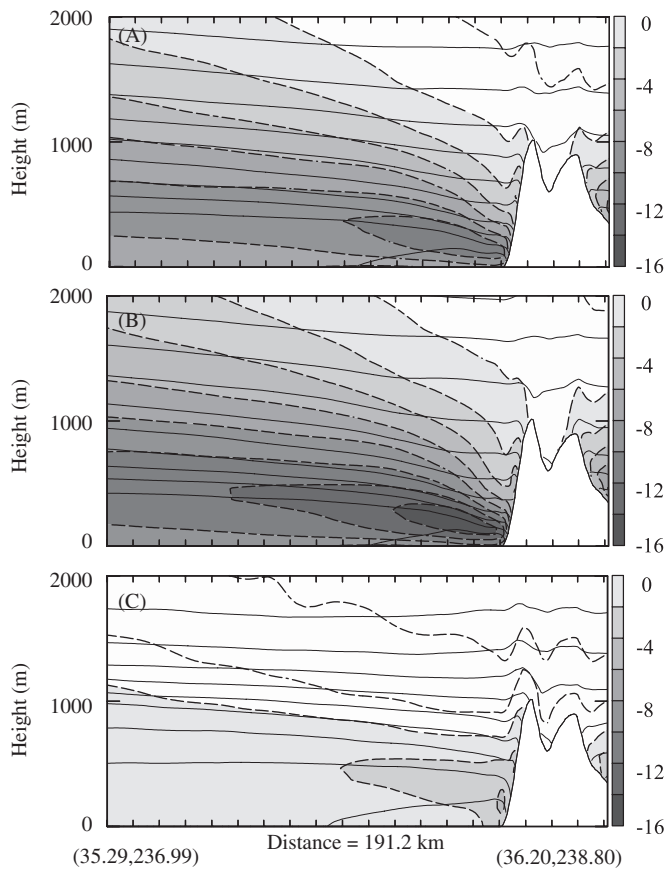
Fig. 11. Vertical cross section of the potential temperature (interval every 2 K) and wind speed normal to the cross section plane (gray shading interval 2 m s^{-1}) for the (A) August 2003, (B) upwelling-favorable, and (C) relaxation dominated time periods. The cross section location is shown in Fig. 9A.

much weaker inversion structure and less of a sloping boundary layer particularly nearshore, along with a much weaker coastal jet.

The mean surface-stress fields are shown in Fig. 12. The mean stress for August (Fig. 12A) indicates enhanced maxima in the lee of the Santa Cruz Mountains and downstream of Point Sur. A considerable enhancement to the stress maximum is apparent in the mean fields comprising the upwelling regime (Fig. 12B), particularly in the lee of the capes with a nearly twofold increase in the surface-stress magnitude along the Big Sur coastline relative to the monthly mean. Additionally, a broad stress maximum parallels the coast in the stronger flow periods. During the relaxation periods (Fig. 12C), the stress and stress gradients are considerably reduced.

The stress maxima apparent in the mean conditions for August yield a complex pattern of local maxima and minima in the wind-stress curl, as shown in Fig. 13, which is conducive for coastal upwelling and downwelling. Of particular note are the upwelling favorable regions offshore of the Santa Cruz region and along the Big Sur coastline. It is noteworthy that positive wind-stress curl can augment direct wind-driven coastal upwelling processes, whereas negative wind-stress curl can induce downwelling (e.g., Pickett and Paduan, 2003; Capet et al., 2004). The most prominent regions of positive stress curl are along the immediate Central California coastline and cutting across the Monterey Bay. During AOSN-II a research aircraft was used by NPS to perform boundary layer measurements (see Ramp et al., 2008). The wind, wind stress and wind-stress curl were derived from the aircraft observations and a comparison with the COAMPS simulations for
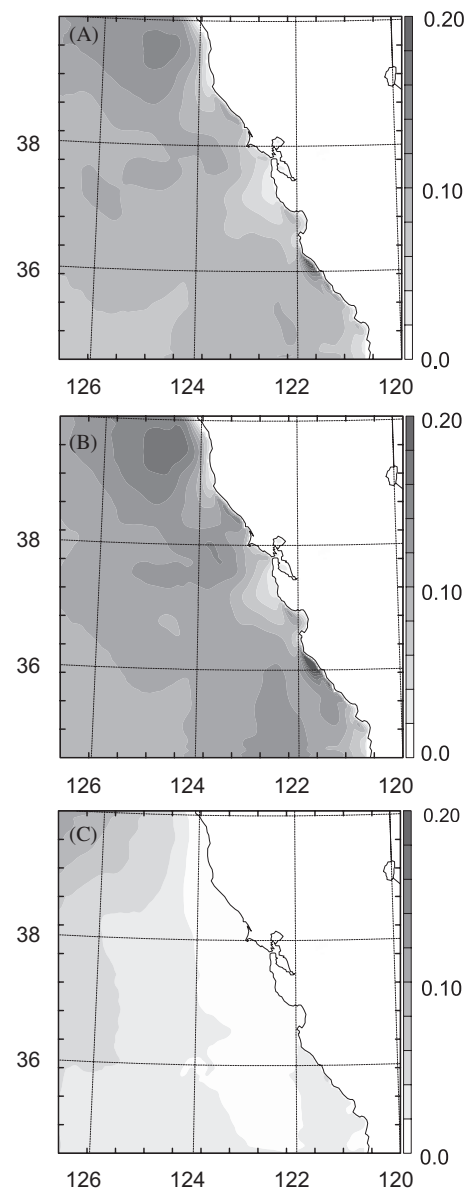
Fig. 12. The surface wind stress (N m^{-2}) for the (A) August 2003, (B) upwelling-favorable, and (C) relaxation dominated time periods for the fourth grid mesh (3-km resolution). The shading interval is 0.02 N m^{-2}.

an upwelling and relaxation event are shown in Fig. 3 of Ramp et al. (2008). The modeled wind and stress fields compare quite favorably with the observations for both the upwelling and relaxation cases examined. Furthermore, it should be noted that the 3-km resolution wind stress and wind-stress curl fields are more accurate, particularly near the coast, relative to the 9-km resolution grid (J. Paduan, personal communication). A more detailed comparison between the observed and model forecasted stresses is the subject of a follow-on study.

The mean surface sensible heat flux for August 2003, shown in Fig. 14A, indicates weakly positive heat fluxes in the Monterey Bay region. The flux pattern is similar in the upwelling-favorable regime (Fig. 14B) and also indicates the presence of downward fluxes in the upwelling-favored regions, which is not surprising since the sea-surface temperatures can be reduced to values lower than the boundary-layer temperatures through the upwelling processes. During the relaxation flow periods (Fig. 14C), the mean sensible heat flux is small.
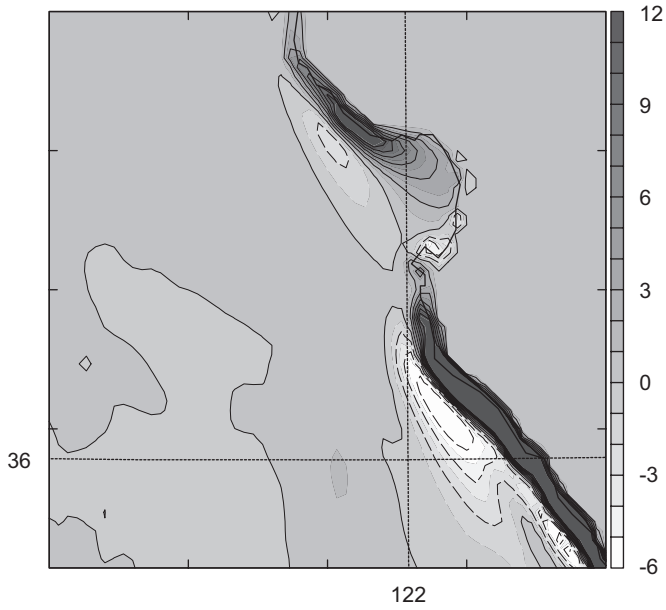
Fig. 13. The mean surface wind-stress curl (10^{-6} N m^{-3}). The shading interval is 1×10^{-6} N m^{-3} and contour interval is 2×10^{-6} N m^{-3}. A sub-domain of the 3-km mesh is shown for clarity.

5. Summary and conclusions

A high-resolution nested non-hydrostatic mesoscale modeling system, COAMPS, was employed during the AOSN-II field campaign to provide surface fields to force a suite of ocean models (e.g., Chao et al., 2008; Shulman and Paduan, 2008; Wang et al., 2008; Ramp et al., 2008). Four horizontally nested grids were used with a minimum resolution of 3 km and 40 vertical layers to properly resolve the mesoscale flow along the Central California coast. Forecasts were performed for a 72-h duration twice daily during August 2003 using an incremental update data assimilation system that made use of a comprehensive set of surface, radiosonde, aircraft, and satellite observations. The forecasts were then disseminated in real time via the internet to the various AOSN-II ocean modeling partners.

The COAMPS results were evaluated and verified using a variety of observational platforms including the available buoys in the AOSN-II Monterey Bay region, namely the MBARI Monterey Bay (46092 and 46093), NOAA Monterey Bay (46042), NOAA Half Moon Bay (46012), and NOAA San Francisco (46026) moorings. The buoy time series indicates that cyclical variations are apparent on the synoptic-scale. These variations govern periods of strong low-level northwesterly winds along the coast that are associated with ocean upwelling-favorable conditions and periods of weak flow or relaxation conditions associated with the cessation of coastal ocean upwelling. The relaxation conditions are characterized by weak pressure gradients near the coast. The model appears to accurately capture these larger-scale transitions between the strong and weak flow periods that each last multiple days in duration. On the shorter time scale, diurnal variations in the strength of the multi-scale sea breeze circulation, which is superimposed on the strong northwesterly flow, are apparent. The buoys located farthest from the coast, 46042 and 46012, indicate the weakest diurnal signatures, while the nearshore buoy, 46092, exhibits the strongest diurnal variations, consistent with our expectations based on sea-breeze dynamics. The COAMPS forecasts accurately capture the differences in the strength of the diurnal cycle between the offshore and near-shore buoys.
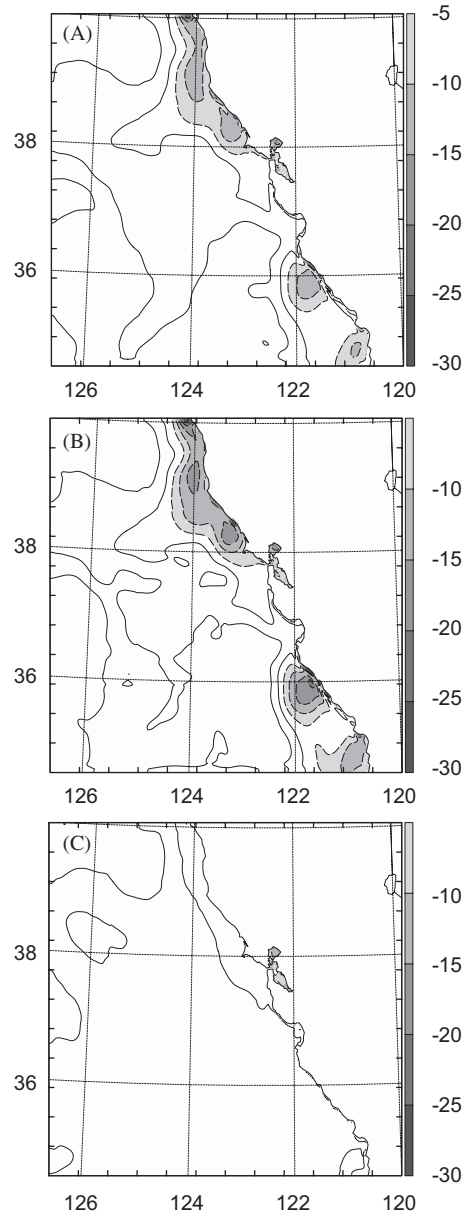
Fig. 14. The surface sensible heat flux (W m^{-2}) for the (A) August 2003, (B) upwelling-favorable and (C) relaxation dominated time periods for the fourth grid mesh (3-km resolution). The contour interval is 5 W m^{-2}.

Additionally, overall the model realistically produces the sea-breeze modulation in the wind speed, although there are periods when the model produces too strong of flow at night during the more quiescent periods. The low-level air temperatures appear to be too warm during some periods, particularly near the transitions between strong and weak flow, which are likely related to an underprediction of low-level clouds.

The bias and RMS error statistics were computed using the buoy data and the 72-h twice daily forecasts for August 2003. The statistics indicate that the model RMS and bias errors were low, particularly for the wind speed and direction throughout the AOSN-II campaign. The overall wind speed bias was typically less than 1 m s^{-1}. Although there were periods when the model predicted low-level temperatures were too warm relative to the buoy observations, the overall bias error statistics were less than 1 °C. The error growth is quite gradual throughout the 72-h forecast periods, perhaps an indication of the low-level control of the land-sea processes on error growth and predictability.

The high-resolution mesh provides more accurate wind-speed variances during the upwelling periods in the nearshore region at the M1 buoy, where the wind-speed gradients and diurnal variations are the largest.

Diagnostics have been performed to obtain a characterization of the mean conditions during the AOSN-II field campaign as well as the conditions associated with the upwelling-favorable and relaxation periods. The periods of strong along-shore winds in the low levels were associated with a mid-tropospheric trough and jet stream that was substantially stronger than the overall mean monthly conditions. During the relaxation periods, the trough was weaker than the mean conditions with a closed low west of the coast that resulted in southerlies near the coast. The mean conditions in the vicinity of the Monterey Bay were characterized by a sloping inversion layer and shallow marine layer near the coast. During upwelling-favorable conditions, the inversion was substantially stronger than during the relaxation periods. The surface-stress field shows maxima in the lee of prominent coastal capes and topography, particularly during the periods of strong low-level flow. The mean stress maxima lead to persistent maxima and minima in the stress curl pattern that create a complex coastal upwelling environment. Regions of positive wind-stress curl, which can augment direct wind-driven coastal upwelling processes, are positioned along Central California coastline and present in the Monterey Bay. Clearly the surface stress forcing arising from the interplay between the large-scale conditions and the complex coastline and terrain is an important issue. The predictability of this complex coastal coupled system remains largely unexplored.

In summary, the results of this study highlight the promising capabilities of high-resolution atmospheric models that can skillfully resolve the flow around and over prominent coastal geometries and topographic features. The resulting complex wind-stress curl pattern is consistently favorable for upwelling conditions along the coast and in particular in the lee of coastal promontories. Although it is difficult to demonstrate statistical superiority of the 3-km mesh relative to the 9-km grid, a qualitative examination of the forecasts indicate that the 3-km mesh contains more realistic structures in the low-level wind, temperature, and the related flux fields along the coastline. Creation of long-term model datasets at high resolution will be excellent testbeds to explore the significance of high-resolution atmospheric forcing on the coastal ocean circulation. Field campaigns such as AOSN-II will be critical to provide the necessary observations to evaluate the ocean and atmospheric models and ultimately the high-resolution mesoscale coupled systems.

Acknowledgments

References

Baldwin. M.E., Lakshmivarahan, S., Kain, J.S., 2002. Development of an "events-oriented" approach to forecast verification. Preprints, 19th Conference on Weather Analysis and Forecasting, American Meteorological Society, San Antonio, TX, pp. 255–258.

Banta, R.M., Olivier, L.D., Levinson, D.H., 1993. Evolution of the Monterey Bay sea-breeze layer as observed by pulsed Doppler lidar. Journal of Atmospheric Science 50, 3959–3982.

Beardsley, R.C., Dorman, C.E., Friehe, C.A., Rosenfeld, L.K., Winant, C.D., 1987. Local atmospheric forcing during the Coastal Ocean Dynamics Experiment, 1. A description of the marine boundary layer and atmospheric conditions over a northern California upwelling region. Journal of Geophysical Research 92, 1467–1488.

Bond, N.A., Mass, C.F., Overland, J.E., 1996. Coastally trapped wind reversals along the United States west coast during the warm season. Part 1: climatology and temporal evolution. Monthly Weather Review 124, 430–445.

Bosart, L.F., 1983. Analysis of a California Catalina eddy event. Monthly Weather Review 111, 1619–1633.

Burk, S.D., Thompson, W.T., 1996. The summertime low-level jet and marine boundary layer structure along the California coast. Monthly Weather Review 124, 668–686.

Burk, S.D., Thompson, W.T., Haack, T., 2000. The dynamics of wave clouds upwind of coastal orography. Monthly Weather Review 128, 1438–1455.

Capet, X.J., Marchesiello, P., McWilliams, J.C., 2004. Upwelling response to coastal wind profiles. Geophysical Research Letters 31, L13311.

Chao, Y., Li, Z., Kindle, J.C., Paduan, J.D., Chavez, F.P., 2003. A high-resolution surface vector wind product for coastal oceans: blending satellite scatterometer measurements with regional mesoscale atmospheric model simulations. Geophysical Research Letters 30, 1013.

Chao, Y., Li, Z., Farrara, J., McWillliams, J.C., Bellingham, J., Caper, X., Chavez, F., Choi, J.-K., Davis, R., Doyle, J.D., Frantaoni, D., Li, P., Marchesiello, P., Moline, M.A., Paduan, J., Ramp, S., 2008. Development, implementation and evaluation of a data-assimilative ocean forecasting system off the central California coast. Deep Sea Research II, this issue [doi:10.1016/j.dsr2.2008.08.011].

Cui, Z., Tjenrström, M., Grisogono, B., 1998. Idealized simulations of atmospheric coastal flow along the central coast of California. Journal of Applied Meteorology 37, 1332–1363.

Darby, L.S., Banta, R.M., Pielke, R.A., 2002. Comparisons between mesoscale model terrain sensitivity studies and Doppler lidar measurements of the sea breeze at Monterey Bay. Monthly Weather Review 130, 2813–2838.

Dorman, C.E., Enriquez, A.G., Friehe, C.A., 1995. Structure of the lower atmosphere over the northern California coast during winter. Monthly Weather Review 123, 2384–2404.

Dorman, C.E., Rogers, D.P., Nuss, W., Thompson, W.T., 1999. Adjustment of the summer marine boundary layer around Pt. Sur, California. Monthly Weather Review 127, 2143–2159.

Dorman, C.E., Holt, T., Rogers, D.P., Edwards, K., 2000. Large-scale structure of the June–July 1996 marine boundary layer along California and Oregon. Monthly Weather Review 128, 1632–1652.

Enriquez, A.G., Friehe, C.A., 1995. Effects of wind stress and wind stress curl variability on coastal upwelling. Journal of Physical Oceanography 25, 1651–1671.

Haack, T., Burk, S.D., Dorman, C., Rogers, D., 2001. Supercritical flow interaction within the Cape Blanco–Cape Mendocino orographic complex. Monthly Weather Review 129, 688–708.

Haley Jr., P.J., Lermusiaux, P.F.J., Robinson, A.R., Leslie, W.G., Logoutov, O., Cossarini, G., Liang, X.S., Moreno, P., Ramp, S.R., Doyle, J.D., Bellingham, J., Chavez, F., Johnston, S., 2008. Forecasting and reanalysis in the Monterey Bay/California current region for the Autonomous Ocean Sampling Network-II Experiment. Deep-Sea Research II, this issue [doi:10.1016/j.dsr2.2008.08.010].

Hodur, R.M., 1997. The Naval Research Laboratory's coupled ocean/atmosphere mesoscale prediction system (COAMPS). Monthly Weather Review 125, 1414–1430.

Hodur, R.M., Doyle, J.D., 1998. The coupled ocean/atmosphere mesoscale model prediction system (COAMPS). Coastal ocean prediction. Coastal and Estuarine Studies 56, 125–155.

Kalnay, E., Kanamitsu, M., Kistler, R., Collins, W., Deaven, D., Gandin, L., Iredell, M., Saha, S., White, G., Woollen, J., Zhu, Y., Leetmaa, A., Reynolds, B., Chelliah, M., Ebisuzaki, W., Higgins, W., Janowiak, J., Mo, K.C., Ropelewski, C., Wang, J., Jenne, R., Joseph, D., 1996. The NCEP/NCAR 40-year reanalysis project. Bulletin of American Meteorological Society 77, 437–472.

Kindle, J.C., Hodur, R., deRada, S., Paduan, J., Rosenfeld, L., Chavez, F., 2002. A COAMPS reanalysis for the Eastern Pacific: properties of the diurnal sea breeze along the central California coast. Geophysical Research Letter 29 (24), 2203.

Koračin, D., Dorman, C.E., Dever, E.P., 2004. Coastal perturbations of marine-layer winds, wind stress, and wind stress curl along California and Baja California in June 1999. Journal of Physical Oceanography 34, 1152–1173.

Marchesiello, P., McWilliams, J.C., Shchepetkin, A., 2003. Equilibrium structure and dynamics of the California current system. Journal of Physical Oceanography 33, 753–783.

Nachamkin, J.E., 2004. Mesoscale verification using meteorological composites. Monthly Weather Review 132, 941–955.

Nachamkin, J.E., Chen, S., Schmidt, J., 2005. Evaluation of heavy precipitation forecasts using composite-based methods: a distributions-oriented approach. Monthly Weather Review 133, 2163–2177.

Nachamkin, J.E., Cook, J., Frost, M., Martinez, D., Sprung, G., 2007. Evaluation of dispersion forecasts driven by atmospheric model output at coarse and fine resolution. Journal of Applied Meteorology 46, 1967–1980.

Pickett, M.H., Paduan, J.D., 2003. Ekman transport and pumping in the California current based on the US Navy's high-resolution atmospheric model (COAMPS). Journal of Geophysical Research 108, 3327.

Ramp, S.R., Davis, R.E., Leonard, N.E., Shulman, I., Chao, Y., Robinson, A.R., Marsden, J., Lermusiaux, P., Fratantoni, D., Paduan, J.D., Chavez, F., Bahr, F.L., Liang, S., Leslie, W., Li, Z., 2008. Preparing to predict: the second Autonomous Ocean Sampling Network (AOSN-II) Experiment in the Monterey Bay. Deep-Sea Research II, this issue [doi:10.1016/j.dsr2.2008.08.013].

Rogers, D.P., et al., 1998. Highlights of coastal waves 1996. Bulletin of American Meteorology Society 79, 1307–1326.

Rogerson, A.M., 1999. Transcritical flows in the coastal marine atmospheric boundary layer. Journal on Atmospheric Science 56, 2761–2779.

Samelson, R.M., 1992. Supercritical marine-layer along a smoothly varying coastline. Journal on Atmospheric Science 49, 1571–1584.

Samelson, R.M., et al., 2002. Wind stress forcing of the Oregon coastal ocean during the 1999 upwelling season. Journal of Geophysical Research 107, 3034.

Shulman, I., Paduan, J.D., 2008. Assimilation of HF radar-derived radials and total currents in the Monterey Bay area. Deep Sea Research II, this issue [doi:10.1016/j.dsr2.2008.08.004].

Shulman, I., Kindle, J., Martin, P., de Rada, S., Doyle, J., Penta, B., Anderson, S., Chavez, F., Paduan, J., Ramp, S., 2007. Modeling of upwelling/relaxation events using the Navy Coastal Ocean Model. Journal of Geophysical Research 112, C06023, doi:10.1029/2006JC003946.

Thompson, W.T., Haack, T., Doyle, J.D., Burk, S.D., 1997. A nonhydrostatic mesoscale simulation of the 10–11 June 1994 coastally trapped wind reversal. Monthly Weather Review 125, 3211–3230.

Thompson, W.T., Burk, S.D., Lewis, J., 2005. Fog and low clouds in a coastally trapped disturbance. Journal of Geophysical Research 110, D18213.

Tjernström, M., Grisogono, B., 2000. Simulations of supercritical flow around points and capes in a coastal atmosphere. Journal on Atmospheric Science 57, 108–135.

Wang, X., Chao, Y., Dong, C., Farrara, J., Li, Z., McWilliams, J.C., Paduan, J.D., Rosenfeld, L.K., 2008. Modeling tides in Monterey Bay, California. Deep Sea Research II, this issue [doi:10.1016/j.dsr2.2008.08.012].

Winant, C.D., Dorman, C.E., Friehe, C.A., Beardsley, R.C., 1988. The marine layer off northern California: an example of supercritical channel flow. Journal on Atmospheric Science 45, 3588–3605.